Stress Control of Dike Deflection and Flank Eruption at Akaroa Volcano, New Zealand

Robert T. Goldman[1] , John A. Albright[1] , Darren M. Gravley[2], Eric B. Grosfils[3] , Patricia M. Gregg[1] , and Samuel J. Hampton[2]

[1]Department of Geology, University of Illinois at Urbana-Champaign, Urbana, IL, USA, [2]School of Earth and Environment, University of Canterbury, Christchurch, New Zealand, [3]Geology Department, Pomona College, Claremont, CA, USA

Abstract Understanding the stress evolution of extinct volcanoes can improve efforts to forecast flank eruptions on active systems. Field, petrographic, and seismic data are combined with numerical modeling to investigate the paleo-stress field of New Zealand's Akaroa Volcano, or Akaroa Volcanic Complex. Field mapping identifies 86 radially oriented dikes and seven lava domes found only within a narrow elevation range along Akaroa's erosional crater rim. These observations suggest that crater rim dike emplacement resulted from lateral deflection of vertically ascending intrusions from a centralized magma source, which in turn may have facilitated formation of the lava domes, as well as two scoria cones. We postulate that dike deflection occurred along a stress barrier, as neither a compositional change nor structural boundary are present. We use a finite element model (FEM) simulating Akaroa to test how different factors may have influenced the system's stress state and dike geometry. Elastic, non-flexural ("roller") model configurations containing a large, oblate, and shallow magma chamber produce stress barriers most conducive to radial dike emplacement along Akaroa's crater rim. These configurations also simulate rapid edifice construction above a preexisting lithospheric "bulge." Conversely, simulating flexural stresses exerted on the lithosphere by Akaroa's large mass hinder rather than promote radial dike emplacement. Temperature-dependent viscoelastic relaxation promotes gradual increases in stress barrier elevation, though this effect is strongly dependent on magma chamber parameters. These results suggest that Akaroa was constructed rapidly (within ~100 kyr) prior to crater rim dike emplacement, which occurred throughout the volcano's remaining active lifespan.

Plain Language Summary Fully understanding how magma moves within active volcanoes requires scientists to study solidified remnants of once-molten magma "plumbing systems" that have been unearthed by the erosion of extinct (i.e., no longer active) volcanoes. Here we present new observations of New Zealand's Akaroa Volcano, an extinct volcanic mountain or "edifice" built from lava eruptions and underground magma movement that occurred in multiple regions rather than one central summit vent. Observations include on-the-ground measurements of rock formations, microscope analysis of rock samples, satellite-derived elevation data, and underground properties inferred from earthquake-generated seismic waves. We incorporate these observations into a computer model of the once-active volcano to understand why magma followed the paths it did, erupting on Akaroa's sides, or flanks, rather than its central summit region. Based on the results of our computer model, these eruptions occurred throughout Akaroa's one-million-year lifespan, after the volcano itself was constructed in the geologically "brief" period of roughly 100,000 years. Our computer simulations also provide a framework for improving scientists' assessments of future eruption risks on the slopes of active volcanoes with a similar shape and chemical composition to Akaroa, such as Sicily's Mt. Etna or the Galapagos' Fernandina volcano.

1. Introduction

Predicting volcanic eruption locations is critical for hazard assessment and prevention. Flank eruptions, which are fed by magmatic intrusions that often propagate several kilometers from a central vent before breaching the surface, are among the most common and societally disruptive type of volcanic event. In May 2021, for example, the eruption of at least two lava fissures on the lower southern slope of Nyiragongo volcano destroyed roughly 1,000 homes, displaced about 25,000 residents, and killed over 30 people in the Democratic Republic of the Congo (Global Volcanism Program, 2021b). Four months later, a dike-fed eruption on the southern slope of La Palma volcano in Spain's Canary Islands required the evacuation of over 5,000 people and destroyed over 100 buildings (Global Volcanism Program, 2021a). In 2018, the largest eruption of Hawaiʻi's Kīlauea Volcano in

Investigation: Robert T. Goldman, John A. Albright, Darren M. Gravley, Samuel J. Hampton
Methodology: Robert T. Goldman, John A. Albright, Darren M. Gravley, Eric B. Grosfils, Patricia M. Gregg, Samuel J. Hampton
Project Administration: Robert T. Goldman, John A. Albright
Resources: Darren M. Gravley, Eric B. Grosfils, Patricia M. Gregg, Samuel J. Hampton
Software: Robert T. Goldman, John A. Albright, Eric B. Grosfils, Patricia M. Gregg
Supervision: Darren M. Gravley, Eric B. Grosfils, Patricia M. Gregg, Samuel J. Hampton
Validation: Robert T. Goldman, John A. Albright, Eric B. Grosfils, Patricia M. Gregg
Visualization: Robert T. Goldman, John A. Albright
Writing – original draft: Robert T. Goldman
Writing – review & editing: Robert T. Goldman, John A. Albright, Darren M. Gravley, Eric B. Grosfils, Patricia M. Gregg, Samuel J. Hampton

over 200 years produced 24 dike-fed fissures that erupted lava flows covering over 35 km^2 of land, requiring the evacuation of roughly 2,500 residents and destroying over 700 buildings (Williams et al., 2020).

Flank eruptions increase the area of an active volcano that volcanologists must monitor for signs of unrest. However, understanding the factors governing intrusion formation and propagation can potentially reduce the spatial uncertainty of eruption forecasts. The magnitude and orientation of stresses acting within a volcano typically control where active intrusions will propagate (Anderson, 1939; Nakamura, 1977; Rubin & Pollard, 1987). Thus, gaining improved insight into the stress fields of active volcanoes can lead to improved forecasts of where new flank eruptions will occur. By the same token, observations of solidified intrusions exposed within an ancient, eroded edifice provide insight into how magma moved beneath the subsurface, and thus into how that volcano's stress field was configured when the volcano was active.

Here we use field, petrographic, and seismic data from New Zealand's Akaroa Volcano to constrain elastic and viscoelastic finite element models that simulate the ancient volcano's paleo-stress field. Akaroa provides an ideal system to investigate whether volcanic edifice stress fields can control flank eruptions because of extensive erosion exposing numerous dikes. We focus our investigation on a sequence of radial dikes and lava domes observed around Akaroa's erosional crater rim that occur within a narrow elevation range (Figure 1; Forsyth et al., 2008). We infer that the lava domes were fed by the compositionally related radial dikes, and thus postulate that the locations of both features were controlled by the same mechanism. There is no pervasive field or tomographic evidence of a significant mechanical boundary, of either structural or compositional origin, that could have controlled the emplacement elevation of the dikes and lava domes. Thus, we test the hypothesis that the geometry of the Akaroa edifice created a "stress barrier" (Gudmundsson, 1990; Martí et al., 2017; Poland et al., 2008) that may have deflected vertically ascending feeder dikes laterally away from the (paleo) summit. Some of these deflected dikes may then have erupted to form lava domes that are only observed along the crater rim at elevations 400–600 m above (present-day) sea level (a.s.l.). While vertical dike emplacement is also possible (e.g., Porreca et al., 2006), we limit our focus to testing the viability of lateral deflection. We assume that the pre-erosion summit was located above what is now Akaroa Harbor (Figure 1b) based on the location of a Bouguer gravity anomaly maximum, which suggests an accumulation of dense intrusive rocks, and thus a centralized magma body, beneath the harbor (Dorsey, 1988).

2. Geology of Akaroa Volcano

Akaroa is a large composite volcano with shield-like morphology that formed in the late Miocene between 9.4 and 8 Ma (Sewell, 1988; Timm et al., 2009). Akaroa makes up the southeastern portion of the Banks Peninsula, while the northwestern portion consists of the Lyttelton composite volcano (11.0–9.7 Ma) and several smaller volcanic groups (Hampton & Cole, 2009; Stipp & McDougall, 1968). Both Lyttelton and Akaroa are intraplate volcanoes that likely formed as a result of two distinct episodes of lithospheric delamination (Timm et al., 2009), and each contains a harbor within a large central "erosional caldera" (Stipp & McDougall, 1968; Williams, 1941), which we refer to as a crater rim. While early studies of both volcanoes posited that each formed from a single conical edifice (Sewell, 1988; Shelley, 1987), Hampton and Cole (2009) identify multiple eruptive centers along Lyttelton Volcano and conclude that its central caldera-like morphology resulted from the combined erosion of localized crater rim segments around each of Lyttelton's vents. Similarly, field and remote sensing observations conducted over the last decade suggest that Akaroa's present-day morphology resulted from the erosion of localized crater rim segments, as illustrated in Figure 1a (Hampton & Gravley, 2020). Thus, Akaroa Volcano is also referred to as the Akaroa Volcanic Complex (AVC; Hampton & Gravley, 2020). However, the fact that the AVC's discrete cone sectors overlap to form a single, roughly radially symmetric edifice structure allows us to treat Akaroa as a single volcano (henceforth "Akaroa Volcano") in the numerical model of this study.

Seismic observations indicate that the Akaroa Volcano extends 10s of km offshore (Figure 1) and is underlain by a conical "bulge" of basement material that is elevated 870 m above its typical depth. This bulge is part of a larger swell, roughly 70 km in diameter, that exists beneath the entire Banks Peninsula and elevates the basement by as much as 1 km beneath Lyttelton Volcano relative to the Canterbury Plains (Lee et al., 2017; Figure 12). The basement is overlain by two additional sedimentary units with an average combined thickness of roughly 200 m that follow the dip of the basement's upper boundary. Although our study does not directly simulate the bulge's formation, given the dip of the overlying sediment we assume that it occurred prior to construction of Akaroa
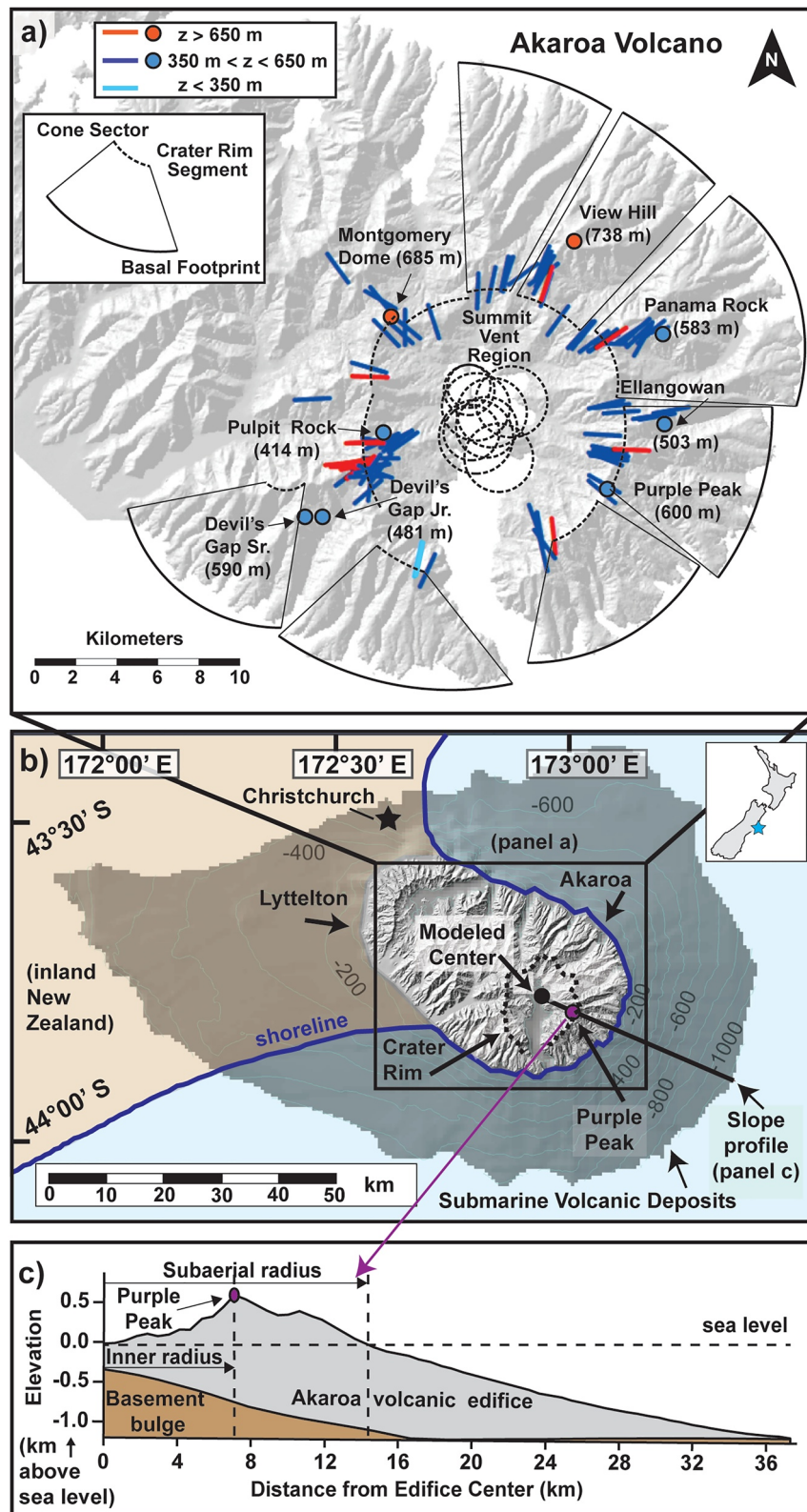
Figure 1.

Volcano. We reflect on two possible mechanisms for how the bulge formed in our Discussion, given its influence on the elevation and slope-parallel dip of the stress barrier simulated in most of this study's numerical model configurations (Section 4).

Akaroa's volcanism consists of a bimodal distribution of basaltic and trachytic deposits. These include widespread basaltic lava flows, scoria cones distributed throughout the volcano, and lava domes concentrated along Akaroa's erosional crater rim (Hampton & Gravley, 2020). Trachyte magmatism and its associated lava dome eruptions were originally considered to be late-stage events in the construction of Akaroa Volcano (Dorsey, 1988). This interpretation was further explored by Hartung (2011), who postulated that the compositional "gap" between basaltic and trachytic magmas was caused by extraction of two spatially and temporally distinct magma bodies from an evolving crystal mush located at depths of 10–20 km. By contrast, Bertolett (2019) provides geochemical, cathodoluminescence, field, and petrologic evidence for a multi-compositional, shallow crustal magma plumbing system that fed cyclic eruptions of basalt and trachyte on Akaroa.

The rate of Akaroa Volcano's construction may have been as rapid as 0.1–0.3 Ma (Stipp & McDougall, 1968) or as long as 1 Ma (Timm et al., 2009). However, evidence for rapid growth is limited to one K/Ar age for a single hawaiite lava dome belonging to the contemporaneous, but magmatically distinct, Mt. Herbert volcanic group located between Lyttelton and Akaroa (9.7–8 Ma, Sewell, 1988). Conversely, the 1 Ma growth proposed by Timm et al. (2009) is supported by $^{40}Ar/^{39}Ar$ ages obtained from five volcanic rocks sampled from a variety of elevations and regions within Akaroa Volcano.

2.1. Constraining Dike Propagation Paths From Field and Petro-Fabric Observations

Systematic field, geomorphology and petrology data constrain dike propagation paths within the Akaroa edifice. Observations range in scale from tens of kilometers, as in the digital elevation model (DEM; Figure 1), to millimeters, as seen through a petrographic microscope (Figure 2). Comparing topography with field observations (Figure 1) reveals that six trachyte domes, one basalt dome (Montgomery), and one scoria cone (Purple Peak) are concentrated on or near Akaroa's erosional crater rim. Five trachyte domes and the Purple Peak scoria cone exist at elevations from 400 to 600 m a.s.l., while the Montgomery and View Hill lava domes are found above 650 m. One trachyte dome, Panama Rock, was constructed within a partially eroded scoria cone (Lewis & Hampton, 2015). A radial swarm of 86 dikes is also observed around the crater rim perimeter (Figure 1a), consisting of 32 basalt, 48 trachyte, and 6 dikes of unverified composition (Goldman, 2022a, 2022b). Most of these dikes are found between elevations of 350 and 650 m.

The similarities in elevation and composition between the dikes and lava domes or scoria cones of the crater rim suggest that each dome or cone was fed by a radially aligned dike of the same composition. The strongest evidence for dome formation from a radial dike is an ENE-trending trachyte dike that terminates inside of Panama Rock, located 583 m a.s.l. on the northeastern crater rim (Figure 2; Lewis & Hampton, 2015). Two observations suggest that magma transported by this radial dike erupted to feed Panama Rock: the dike terminates inside the dome and there are clear petrologic similarities between the two features (63% silica and a fine-grained trachytic texture dominated by alkali feldspar needles with rare augite and olivine). The eruption of Panama Rock within a partially eroded scoria cone (Lewis & Hampton, 2015) indicates that the same background stress field acted on both the trachytic and basaltic intrusions that fed the dome and cone, respectively.

Field observations of crater rim dikes are complemented by observations of mineral alignment, or petrofabrics, within petrographic thin sections sampled from these dikes. The textural alignment of elongate minerals like plagioclase is often used to constrain magma flow direction within a dike, due to shearing that occurs along the dike's margins and aligns high-aspect-ratio plagioclase crystals into a similar orientation as the original flow direction (Harp & Valentine, 2018; Philpotts & Philpotts, 2007; Poland et al., 2004; Shelley, 1985). However,

Figure 1. (a) Shaded relief map of Akaroa Volcano indicating the observed location and trends of dikes (lines) and locations of lava domes and scoria cones (dots) observed along Akaroa's erosional crater rim. Both sets of features are color-coded by elevation "z" above sea level. Line lengths do not represent actual dike lengths; the midpoint of each line indicates the location and elevation at which exposed dike segments were observed. (b) Shaded relief and bathymetric map of Banks Peninsula. Light gray region is subaerially exposed Banks Peninsula topography, while the dark gray region shows volcanic deposits either submerged beneath the South Pacific Ocean (light blue) or buried beneath Pliocene and Quaternary sediments (light brown). Purple dot: Purple Peak scoria cone. Black dot: Location chosen for the center of this study's numerical model. Data provided by GNS. (c) Elevation profile of the Akaroa edifice and underlying basement based on the seismic model of Lee et al. (2017), measured along the black line in (b). This profile guides the geometry of our numerical simulations (c.f., Supporting Information). The basement slope flattens out at a depth of ~1.2 km below sea level (b.s.l.); depths below this are treated as part of the lithospheric block in our model.
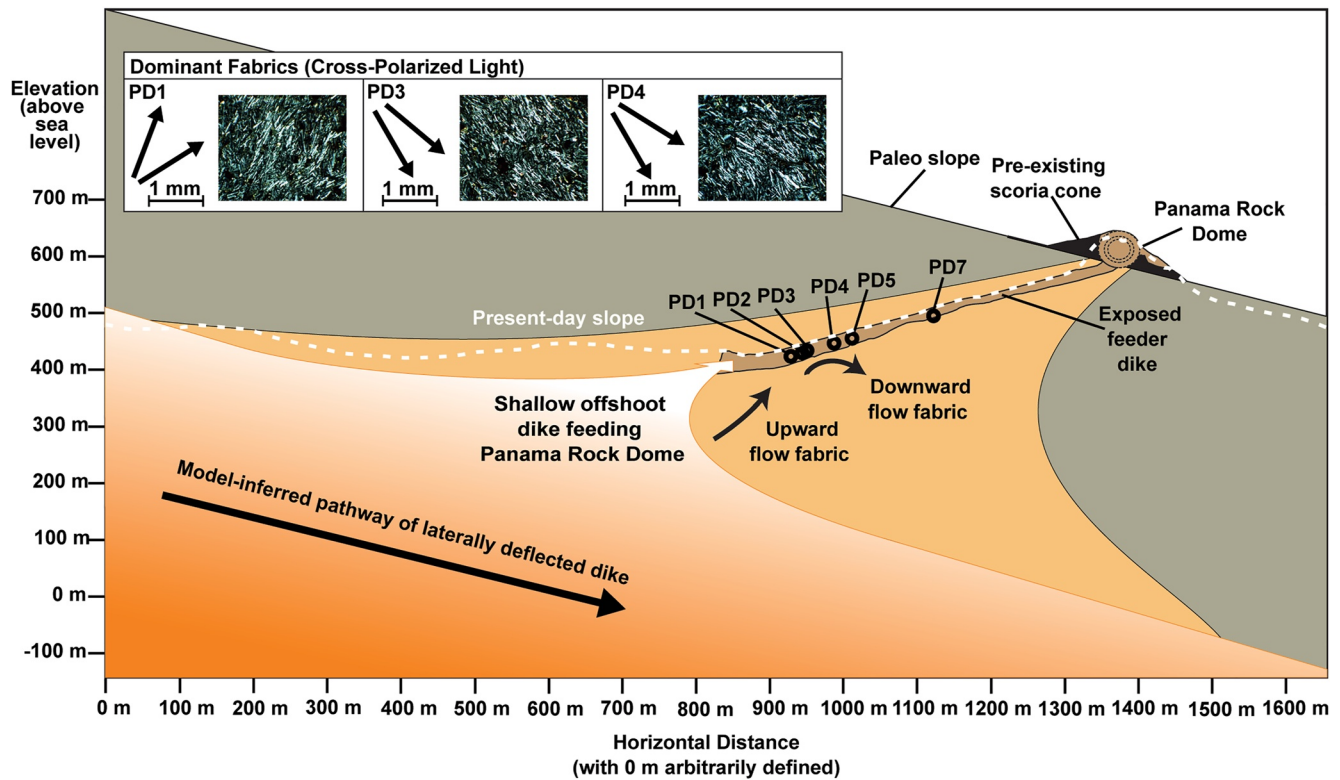
Figure 2. Hypothetical model of feeder dike emplacement and formation of the Panama Rock dome, reflecting Neri et al. (2011, Figure 3a) schematic of lateral dike-fed flank eruptions on Mt. Etna. Sample locations are indicated by black circles along the exposed trachyte feeder dike (brown), with dominant plagioclase fabrics for samples PD1, PD3 and PD4 presented in the top-left corner. Plagioclase minerals are white in the cross-polarized optical microscope images captured with the software *Leica Acquire*.

this shearing decreases with distance away from the margin, meaning that mineral shape preferred orientation near a dike's center may reflect late-stage rather than initial magma propagation direction (Baer & Reches, 1987; Philpotts & Asher, 1994). Thus, we sampled the margins along transects of two well-exposed crater rim dikes to infer the flow directions possible for the entire dike swarm.

At the Panama Rock feeder dike, six trend-parallel oriented samples were collected along the southeastern vertical dike face to determine the radial component of the dike's flow direction. Samples were then petrographically analyzed using an optical microscope and cross-polarizing filter to qualitatively identify plagioclase fabrics, or patterns in the alignment of the long axis of plagioclase crystals observed in thin section, and constrain the dike's flow direction (Figure 2; Table S4 in Supporting Information S1). In the absence of samples collected from other faces of the dike, it was assumed that plagioclase crystals with an elongate, rather than equant, shape have their long axis oriented within the plane of the thin section they are observed on. In one sample, plagioclase laths dip upward and away from Akaroa's centralized region, while in two samples, these laths dip downward from the center (Figure 2). These fabrics are interpreted as preserving two dominant flow directions within the shallow offshoot of a deeper, laterally propagating dike (Figure 2). No consistent orientation was observed in the remaining three samples.

The vertical fabrics observed from the Panama Rock dike are complemented by horizontal fabrics observed in thin sections collected from samples of three well-exposed dikes that cross-cut the Purple Peak scoria cone (Figure S3 in Supporting Information S1). These samples, whose collection and analysis are described in Supporting Information S1, indicate flow directed away from Akaroa's center. This observation is consistent with the hypothesis that crater rim dikes propagated laterally away from a central magma source beneath Akaroa's paleo summit vent region.
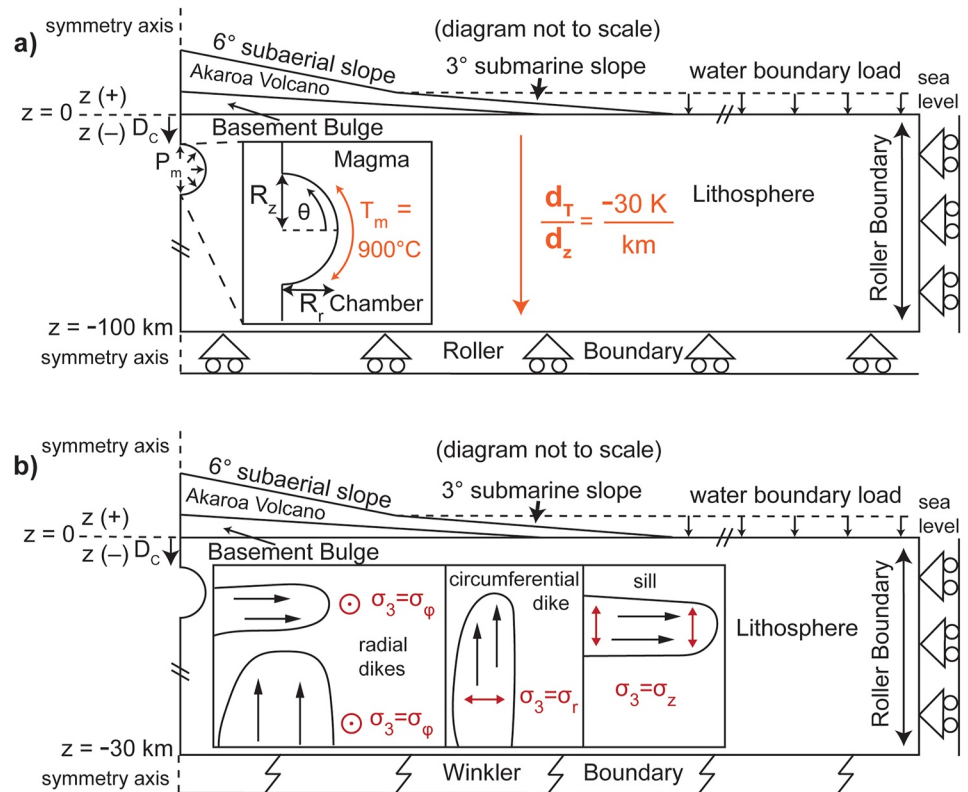
Figure 3. Schematic finite element model diagrams with (a) roller and (b) Winkler (i.e., flexural) basal boundary conditions. These 2D cross-sections are rotated about the central vertical axis to produce an axisymmetric model. Inset in (a) shows magma chamber dimensions and pressurization. The angle θ, measured in the r-z plane counterclockwise from the chamber's mid-depth, denotes the point of greatest tensile stress where the chamber is expected to rupture and produce a new magma intrusion. A constant temperature of 900 °C is applied to the chamber wall, and a background host rock geotherm of -30 K/km is applied to the volcano and lithosphere. Inset in (b) shows geometry of intrusions expected from the three possible orientations of σ_3 (red vectors) used for inferring dike propagation pathways (Figures 5–8). Vectors orthogonal to the axisymmetric model plane, while illustrated here, are not displayed in Figures 5–8.

3. Numerical Approach

A two-dimensional, axisymmetric finite element model (FEM) was developed in *COMSOL Multiphysics 5.5* to estimate the paleo-stress fields within the Akaroa Volcano and underlying lithosphere. The FEM consists of two solid components with distinct material properties inferred from the seismic model of Lee et al. (2017): A conical edifice and the underlying lithosphere (Figure 3). The lithosphere geometry consists of two components: a large cylindrical block representing the elastically deforming region of the lithosphere, and a small cone that sits on top of this cylindrical block, representing the bulge observed beneath the base of Akaroa Volcano (Figure 1c). For convenience, we define z = 0 as the base of the lithospheric bulge (-1.2 km b.s.l.), which also corresponds with the top surface of the cylindrical block of the lithosphere. Approximating Akaroa's shape as a single, axially symmetric cone significantly reduces model computation time, allowing thorough testing of factors which may have influenced the system's stress state and subsequent dike emplacement. Previously published FEM studies (Cabaniss et al., 2018; Del Negro et al., 2009; Galgana et al., 2013; Gregg et al., 2012; Grosfils, 2007; Hurwitz et al., 2009; McGovern et al., 2015) provide a framework for defining the geometry and mechanical behavior of this study's model. FEM parameters are presented in Tables S1 and S2, and variables in Table S3, in Supporting Information S1.

The FEM calculates stresses produced from deformation of the solid model components in response to simultaneous gravitational loading from the volcanic edifice and pressurization of an ellipsoidal void, or magma chamber, representing Akaroa's shallow magma plumbing system. In each model simulation, an outward normal force is applied along the magma chamber wall, increasing its volume until the least compressive principal stress
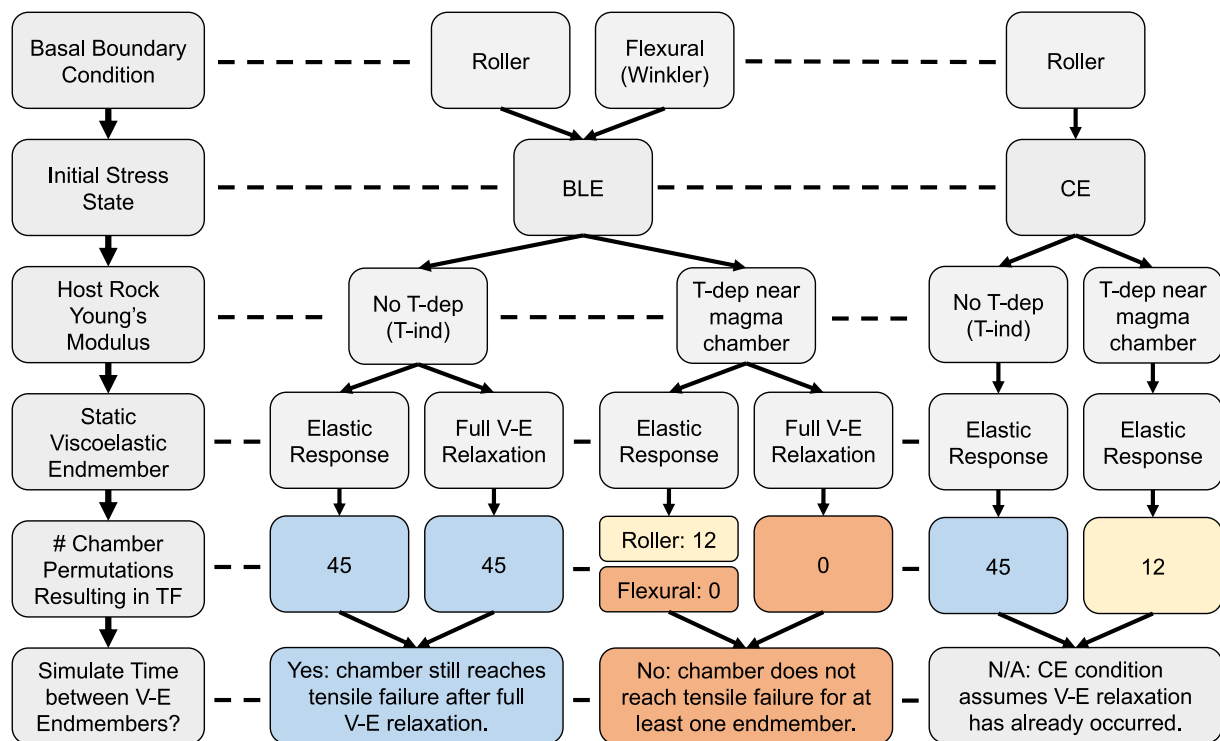
Figure 4. Flow charts of all model configurations examined in this study (BLE = "Bulge-Lithosphere-Equilibrated," CE = "Completely-Equilibrated," TF = "Tensile Failure," V-E = "Viscoelastic," T-dep = "Temperature-dependent," T-ind = "Temperature-independent"). The leftmost column of gray boxes provides a legend for each of the rows of the two flow charts. Unless otherwise specified, the flow chart paths below the BLE box apply to both roller and flexural basal boundary conditions, which produce nearly identical chamber failure outcomes except for the case of both a T-dep Young's modulus and elastic deformation response. CE model configurations only employ a roller basal boundary condition. Boxes are highlighted blue for model configurations where all 45 magma chamber permutations permit tensile failure, yellow where only 12 permit failure, and orange where none result in tensile failure.

σ_3 increases from a negative (compressional) value, following *COMSOL*'s tension-positive sign convention, to 0 MPa anywhere along the chamber wall. The location that first reaches this threshold is assumed to be the site of tensile failure, producing a new intrusion opening perpendicular to σ_3. For the chamber pressure at which tensile failure occurs, a stress field is calculated by the FEM, mapping potential pathways for the emerging intrusion to follow, assuming that chamber pressure remains constant as the intrusion grows. Each path must be inferred from the stress field since the FEM does not simulate crack formation and propagation. Detailed magma pressure calculations are described in Supporting Information S1. The values of chamber pressure and corresponding volume change required for tensile failure in each simulation are available online (Goldman, 2022d).

Stress fields are calculated for numerous geologically plausible configurations of the Akaroa volcanic system. Figure 4 illustrates how the baseline FEM is subdivided by the following parameters (Supporting Information S1): basal boundary condition, initial stress state, temperature dependence of the host rock Young's modulus, and static viscoelastic ("V-E" or "VE") response. Initial stress state is subdivided into bulge-lithosphere-equilibrated (BLE) and completely-equilibrated (CE) endmembers, while host rock Young's modulus is defined as either temperature-independent (T-ind) or temperature-dependent (T-dep) near the magma chamber wall. For each parameter combination, 45 permutations of magma chamber depth ($z = -1, -3, -5$ km; or $D_c = 1, 3, 5$ km), initial volume ($V_m = 1, 5, 15$ km³), and ellipticity ($R_z/R_r = 1/2, 2/3, 1, 3/2, 2$) are simulated (Figure 3 and Table S1 in Supporting Information S1). These values are consistent with geochemically and geophysically-inferred characteristics of shallow magma reservoirs beneath several active basaltic volcanoes—Mt. Etna, Sicily (Albarède, 1993; Lundgren et al., 2003; Neri et al., 2005; Puglisi et al., 2001), Fernandina in the Galapagos (Bagnardi & Amelung, 2012), and Hawai'i's Kīlauea Volcano (Pietruszka & Garcia, 1999). These parameters also correspond with the magma plumbing system of South Korea's Ulleung Island volcano, which, like Akaroa, consists of both basaltic and trachytic volcanic products (Brenna et al., 2014). The fifth row of Figure 4 shows how many of these permutations result in tensile failure of the chamber wall for the specified sequence of FEM
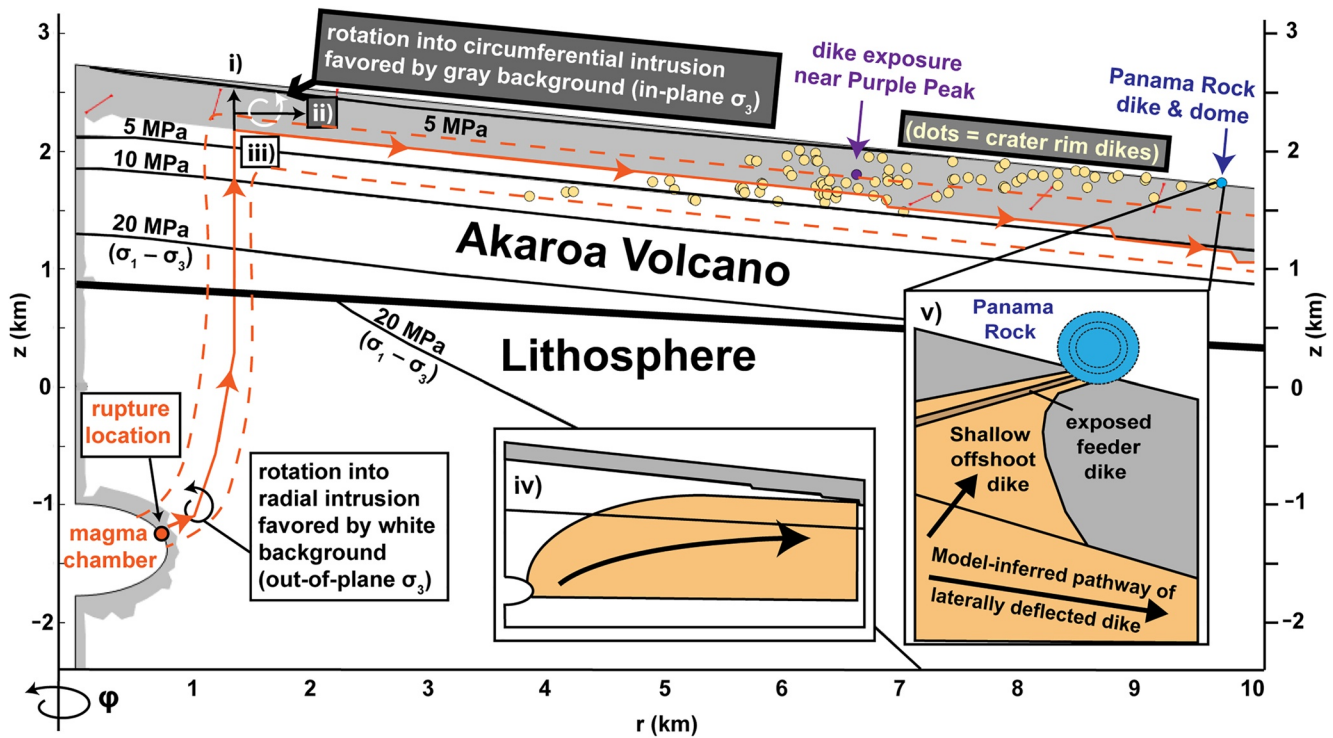
Figure 5. Illustration of how stress field results are interpreted, using a model configuration with a roller basal boundary condition, bulge-lithosphere-equilibrated initial stress state, T-ind host rock Young's modulus, and elastic deformational response. Chamber parameters are $D_c = 1$ km, $V_m = 1$ km^3, and $R_z/R_r = 1/2$. Contours plot the differential stress $\sigma_1 - \sigma_3$. Straight or gently curved arrow segments indicate possible magma intrusion pathways; path segments or panels labeled with lowercase Roman numerals are described in the main text. Circular arrows indicate an intrusion rotating in a direction orthogonal to the radial r-z plane (i.e., the φ-direction, labeled at the bottom of the axis of symmetry).

parameters. Elastic deformation is always simulated in a single ("static") timestep, while viscoelastic deformation is simulated over multiple timesteps if both the initial and final static timesteps permit tensile failure. Since the magma chamber volume change required for tensile failure is similar between the initial and final viscoelastic endmembers (Goldman, 2022d), we fix magma chamber volume to its initial value for tensile failure when calculating the stress field for intermediate timesteps.

4. Modeled Stress Field Results

Stress fields calculated for each model configuration define regions favorable for the propagation of radial or circumferential intrusions (Figures 3 and 5–8). Regions favorable for radial diking have σ_3 oriented orthogonal to the cross-sectional plane (white areas in Figures 5–8), while those favoring circumferential intrusions have σ_3 oriented parallel to this plane (shaded areas in Figures 5–8; Anderson, 1939). Thus, a stress field favoring the emplacement of radial dikes on the flanks of Akaroa Volcano would contain a predominantly white region, extending from locations at depth near the magma chamber wall up toward the shallow regions where crater rim dikes are observed (Figure 5). Likewise, this stress field would be shaded at or above these dike elevations, with the lower boundary corresponding to a "stress barrier" (Gudmundsson, 1990; Martí et al., 2017; Poland et al., 2008) that may have laterally deflected dikes ascending from depth to their observed locations (Figure 5).

Figure 5 illustrates how stress field results are interpreted. The orange dot on the magma chamber wall identifies the first point of rupture ($\sigma_3 = 0$) for magma to emerge as an intrusion. Orange arrows plot one possible path that the leading edge of this intrusion could take, assuming it initially ascends due to magma buoyancy (Rubin, 1995). The differential stress $\sigma_1 - \sigma_3$ indicates how likely the plane of an intrusion will rotate, when crossing the boundary between a shaded and non-shaded region, to reestablish an orientation perpendicular to the σ_3 vectors of the region it has entered. An intrusion entering a region of high differential stress will be more likely to rotate
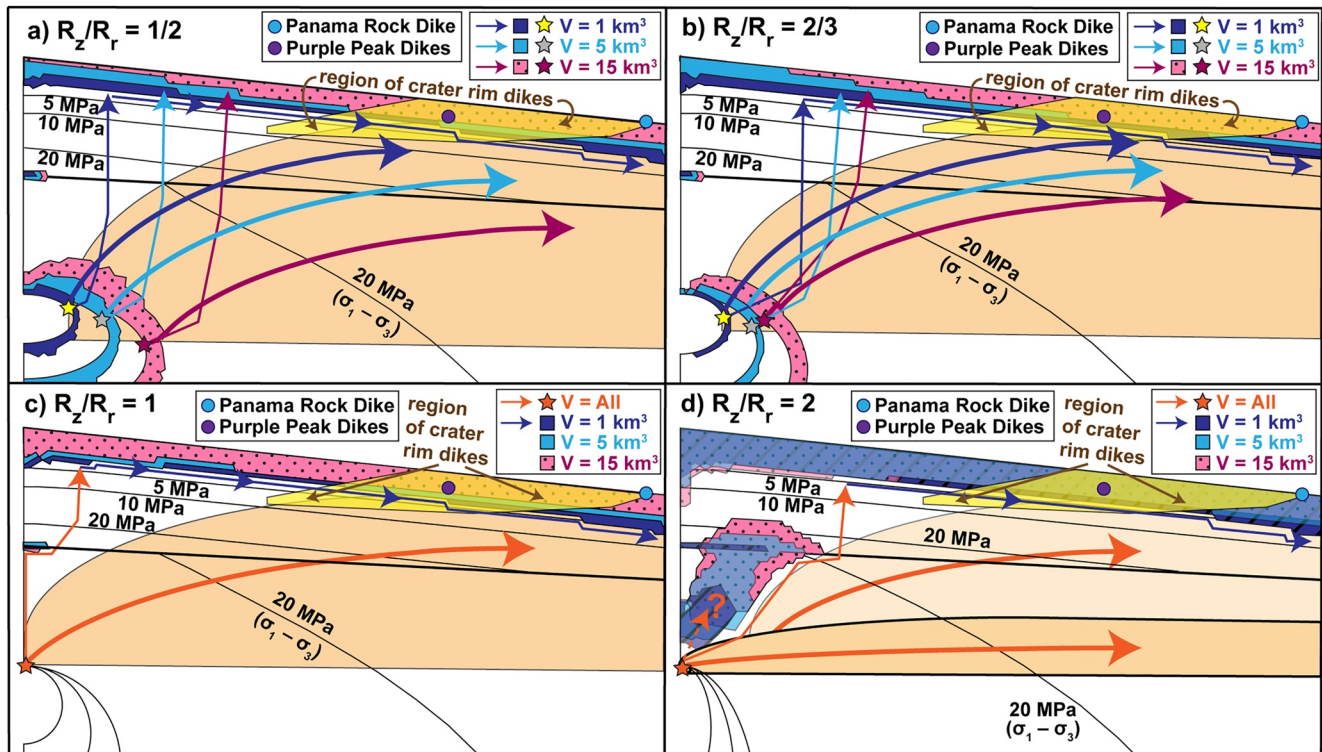
Figure 6. Effect of adjusting magma chamber size and aspect ratio on the stress field of elastic model configurations with a roller basal boundary, bulge-lithosphere-equilibrated pre-stress, and T-ind host rock Young's modulus. Shown are results for initial chamber volumes $V_m = 1, 5, 15$ km³, crest depth $D_c = 1$ km, and chamber aspect ratios R_z/R_r of (a) 1/2, (b) 2/3, (c) 1, and (d) 2. Contours plot the differential stress $\sigma_1 - \sigma_3$ corresponding to the $V = 1$ km³ chamber; results are similar for the other chamber volumes of the same aspect ratio. Panel (d) contains two blade-shaped dike pathways; the lighter beige path represents a potential offshoot of the darker beige path originating from the chamber wall.

sharply over short distances than an intrusion entering a low differential stress region (Chestler & Grosfils, 2013; Mériaux & Lister, 2002).

Yellow dots plotted in the upper right region of Figure 5 are crater rim dike elevations superimposed on the axisymmetric model as a function of their elevation and radial distance from the center of Akaroa Harbor (Goldman, 2022a). The purple dot shows the location of the dike exposure near Purple Peak (Figure 1, Figures S3–S10 in Supporting Information S1), while the blue dot indicates the Panama Rock dike (Figures 1 and 2). In this model configuration, an intrusion exits the point of rupture initially as an inclined sill, since the gray halo around the chamber wall favors circumferential intrusions. After propagating a short distance from the wall, the intrusion rotates into a radially aligned dike, a phenomenon observed at the analogous Fernandina volcano (Bagnardi & Amelung, 2012; Chestler & Grosfils, 2013). This rotation occurs in accordance with the transition of σ_3 from radially aligned (in-plane) to circumferentially aligned (out-of-plane). The dike then ascends toward the surface until reaching a shallow (gray) region within which circumferentially oriented intrusions are favored. From this point, the following scenarios are possible (with lowercase Roman numerals corresponding to Figure 5):

1. Path (i): The dike pushes through the stress barrier to the surface without changing its orientation, if the pressure at the vertical dike tip overcomes external host rock stresses (Corbi et al., 2015; Watanabe et al., 2002) and fracture toughness (Parfitt & Head, 1993; Rubin & Pollard, 1987). This scenario is supported by the low value of differential stress (<5 MPa) near the surface.

2. Path (ii): The dike rotates or "splits" into a sill upon entering the region of radial and vertical σ_3, a phenomenon that has been demonstrated in the analogue models of Galland et al. (2014) for high viscosity magmatic intrusions.

3. Path (iii): The vertical dike tip blunts against the stress barrier, causing the dike to accommodate magmatic pressure by increasing its lateral width until exceeding the lateral host rock fracture toughness (Parfitt &
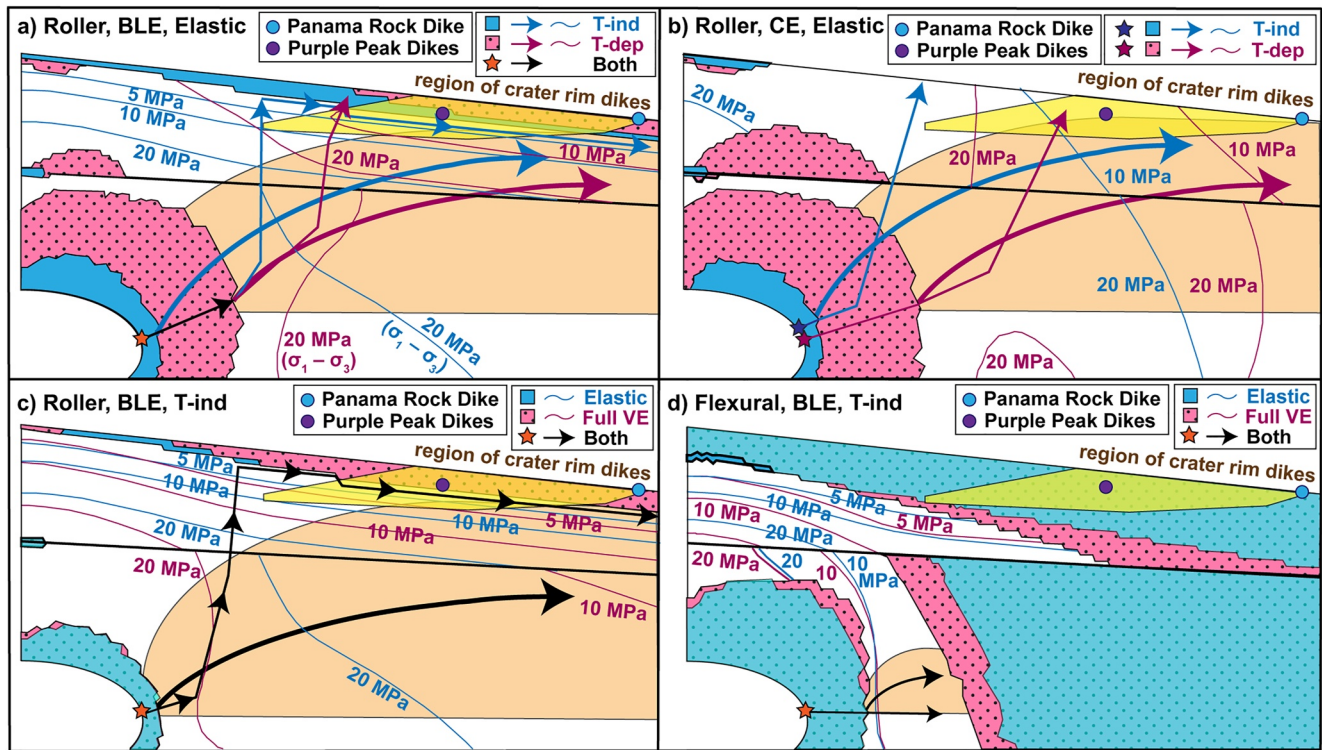
Figure 7. Comparison of stress fields produced by four pairs of model configurations with $D_c = 1$ km, $V_m = 15$ km^3, and $R_z/R_r = 1/2$. (a) T-ind versus T-dep host rock Young's modulus for model with a roller basal boundary, bulge-lithosphere-equilibrated (BLE) pre-stress, and elastic deformation. (b) Same as panel (a) except for a completely-equilibrated (CE) prestress. (c) Elastic deformation versus full viscoelastic (VE) relaxation for a model with a roller basal boundary, BLE pre-stress, and T-ind Young's modulus. (d) Same as panel (c) except for a flexural basal boundary. Though not illustrated directly, intrusions exiting the halo of radial σ_3 around each magma chamber are expected to rotate from circumferentially to radially oriented (c.f., Figure 5).

Head, 1993; Rubin & Pollard, 1987). This would allow the dike to propagate laterally, effectively "deflecting" along the stress barrier.

4. Path (iv): It is also possible for a newly formed dike to propagate both laterally and vertically if its central driving pressure is high enough that stress intensities at its lateral and vertical tips exceed the fracture toughness of the surrounding host rock (Parfitt & Head, 1993; Rubin & Pollard, 1987). In this case, a vertically and laterally propagating dike could be emplaced along the present-day crater rim without the need for deflection along a near-surface stress barrier. In Figure 5, the stress barrier depth is located below the observed elevations of most dikes, including at Purple Peak and Panama Rock. Thus, for dikes to have been emplaced above the stress barrier in the model configuration of Figure 5, they will need to have ascended past the stress barrier, as illustrated in panel (v), after following either path (iii) or (iv).

Key model configurations are summarized in the following subsections and illustrated in Figures 6–8. For these results, dike paths following the same principles as paths (iii) and (iv) in Figure 5 are traced to identify model configurations consistent with the emplacement of radial crater rim dikes. These paths are favored in our analyses since studies of other large composite volcanoes indicate the occurrence of either (a) lateral propagation from a central magma chamber or conduit, or (b) deflection of centrally ascending dikes toward those volcanoes' flanks (Harp, 2021; Neri et al., 2011; Peltier et al., 2005; Porreca et al., 2006). However, due to the erosion of Akaroa's central summit region and the submergence of any intrusions potentially exposed below sea level within Akaroa Harbor, it is not possible to evaluate whether dikes may have followed paths (i) or (ii) of Figure 5.

4.1. Roller Basal Boundary, Bulge-Lithosphere-Equilibrated Pre-Stress, T-Ind Young's Modulus, Elastically Deformed

This first group of FEM configurations yield shallow stress barriers consistent with observed dike elevations (Figures 5 and 6). The existence of a shallow, slope-parallel stress barrier is primarily caused by the similarly
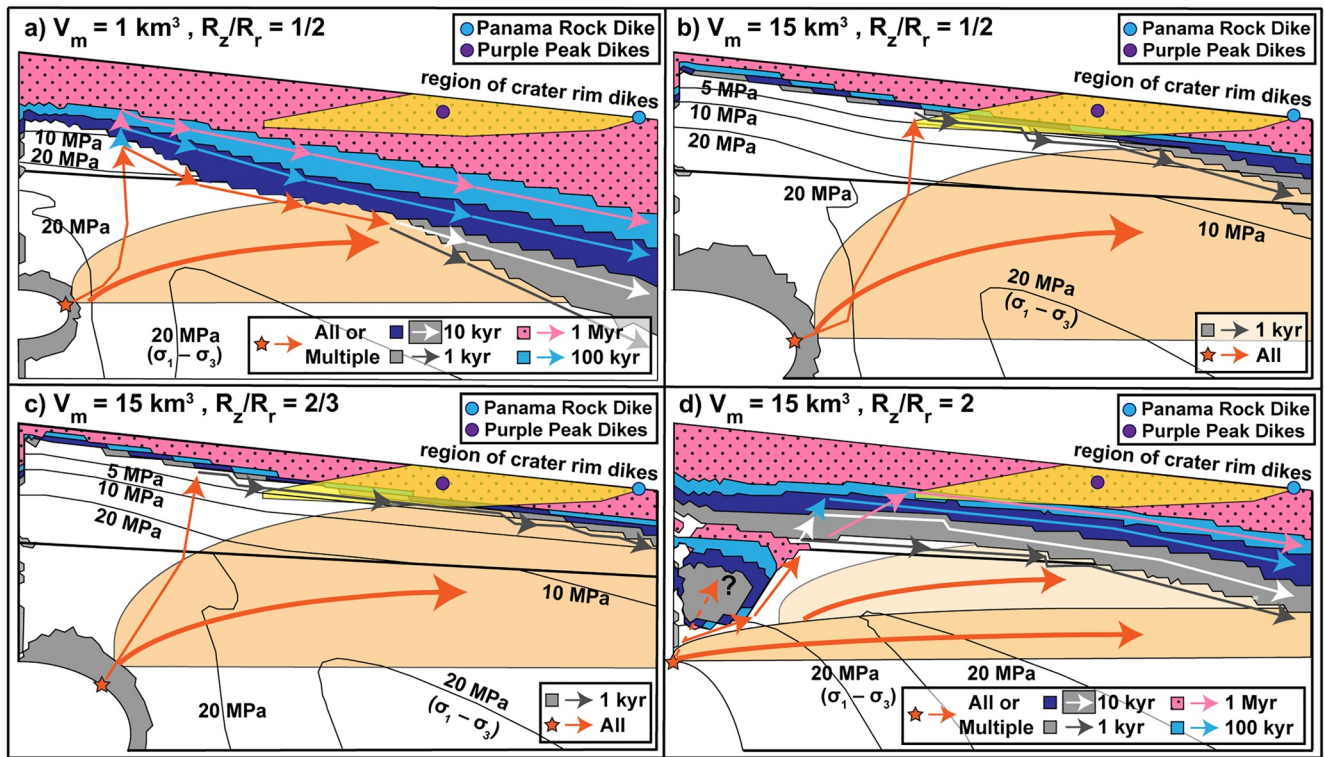
Figure 8. Illustration of the time-dependent evolution in the extent of regions of radial σ_3 for models with a roller basal boundary, bulge-lithosphere-equilibrated pre-stress, T-ind host rock Young's modulus, and T-dep host rock viscosity for the following shallow ($D_c = 1$ km) magma chambers: (a) $V_m = 1$ km^3, $R_z/R_r = 1/2$; (b) $V_m = 15$ km^3, $R_z/R_r = 1/2$; (c) $V_m = 15$ km^3, $R_z/R_r = 2/3$; (d) $V_m = 15$ km^3, $R_z/R_r = 2$. For each configuration, four timesteps are shown: $t = 1$, 10, 100 kyr, and 1 Myr. In panels (b) and (c), the shallow intrusion pathway is only drawn for the 1 kyr timestep since the elevation of the stress barrier does not change significantly for subsequent timesteps. In panel (d), an alternate orange path is drawn illustrating the case of an intrusion entering a region of radial σ_3, similar to Figure 6d. As with Figure 6d, the light beige blade-shaped dike pathway in panel 8d is a potential offshoot from the dark beige path.

sloping boundary marking the contact between Akaroa Volcano's base and the lithospheric bulge. In the absence of this bulge, the volcanic stress field does not permit radial dike propagation at shallow depths (Figure S11 in Supporting Information S1). Magma chamber geometry and depth do not significantly affect stress barrier location near the present-day locations of crater rim dikes (Figure 6, Figure S12 in Supporting Information S1), while increasing chamber size at shallow depth raises stress barrier elevation at these locations (Figure 6). The stress field immediately surrounding oblate magma chambers, which experience tensile failure after volume increases of $1.4–1.7 \times 10^{-3}$ V_m, favors the initial formation of horizontal sills or diagonally inclined circumferential intrusions (Figures 6a and 6b). Due to the high differential stress at depth, sills or circumferential intrusions emerging from oblate chambers are expected to sharply rotate into radial dikes upon entering the white region of circumferentially oriented σ_3.

On the other hand, the stress fields surrounding spherical and prolate chambers, which experience tensile failure after volume increases of $0.2–0.6 \times 10^{-3}$ V_m, favor the emergence of radial dikes without requiring subsequent rotation (Figures 6c and 6d). Each prolate chamber also produces a region of radially oriented σ_3 immediately above the chamber crest, which we interpret as being a deep-seated stress barrier that would have caused radial dikes to deflect in an outwardly ascending diagonal direction (Figure 6d). However, an alternate path is drawn for these prolate chamber configurations illustrating the case of an intrusion entering a region of radial σ_3 (Figure 6d); the question mark indicates that the model does not constrain whether such an intrusion would rotate into a circumferential intrusion (Pansino & Taisne, 2019) or stall without propagating further.

4.2. Roller Basal Boundary, Bulge-Lithosphere-Equilibrated/Completely-Equilibrated Pre-Stress, T-Ind/T-Dep Young's Modulus, Elastically Deformed

Applying a T-dep host rock Young's modulus to elastic model configurations with a roller basal boundary increases the magma chamber volume change required for tensile failure to occur, relative to T-ind configurations (Goldman, 2022d). This results in larger haloes of radially oriented σ_3 surrounding oblate chambers (Figures 7a and 7b). While these haloes favor the formation of sills or circumferential intrusions, radial dike propagation may still be permitted if a sill initiating from the ruptured chamber wall rotated into a radial orientation upon exiting the halo, as suggested by the high values of differential stress existing at depth (Chestler & Grosfils, 2013; Mériaux & Lister, 2002). Roller model configurations with a completely-equilibrated pre-stress (Figure 7b) produce similar stress fields to their bulge-lithosphere-equilibrated counterparts (Figure 7a), except that stress barriers are absent within the first 2–3 km of the summit for completely-equilibrated pre-stress.

4.3. Effects of Full (Single Timestep) Viscoelastic Relaxation or Elastic Flexure, T-Ind Young's Modulus

Complete viscoelastic relaxation of the edifice and lithosphere, when host rock Young's modulus is T-ind, produces small differences in both the chamber volume increase required for tensile failure and the resulting stress field compared with purely elastic deformation (Figures 7c and 7d; Goldman, 2022d). Incorporating a flexural basal boundary, on the other hand, produces a significantly different stress field than a roller basal boundary (Figure 7d). Flexural model stress fields are inconsistent with Akaroa's observed dike geometry, since they contain extensive shaded regions of radially aligned σ_3 that would prevent the lateral propagation of radial dikes along Akaroa's present-day crater rim. As shown in Figure 4, defining a T-dep host rock Young's modulus prevents tensile failure of the magma chamber for any model configuration with either complete viscoelastic relaxation or basal flexure.

4.4. Time-Dependent Viscoelastic Numerical Experiments

Time-dependent viscoelastic model simulations yield significantly different stress field results depending on whether a constant or T-dep viscosity is assigned to the host rock. For simulations with a constant viscosity, the stress field does not change noticeably over time (Figure S13 in Supporting Information S1), consistent with the similarity of the initial elastic and final viscoelastic stress fields (Figures 7c and 7d). For simulations with a T-dep viscosity, the stress barrier elevation falls rapidly within the first 1 kyr, before gradually rising over the remaining 1 Myr of Akaroa's volcanism (Figure 8). The magnitude of stress barrier ascent is strongly controlled by magma chamber size and aspect ratio. Model configurations with a small chamber ($V_m = 1$ km^3) of any aspect ratio do not produce a stress barrier within the region of crater rim dikes for any timestep (Figure 8a), while configurations with a large oblate chamber ($V_m = 15$ km^3) produce a stress barrier along the bottom of this region for all time-steps (Figures 8b and 8c). For a large prolate chamber ($V_m = 15$ km^3, $R_z/R_r = 2$), the stress barrier ascends to the bottom of the region of observed crater rim dikes after 100 kyr (Figure 8d).

5. Discussion

5.1. Optimal Magma Chamber Configuration and Pressurization

Magma chamber size and aspect ratio strongly influence the location of stress barriers observed in bulge-lithosphere-equilibrated, roller basal boundary model configurations (Figures 6 and 7). For these scenarios, all combinations of magma chamber parameters produce stress barriers above or intersecting nearly half of the region where crater rim dikes are observed. However, only the largest ($V_m = 15$ km^3) and most oblate ($a_c = 0.5$, 0.67) chambers produce stress barriers that intersect or exist slightly above the dikes observed near Purple Peak (Figures 6a and 6b, pink shaded regions), due to the large chamber volume increases required for tensile failure (Goldman, 2022d). These large, oblate chambers would also have facilitated emplacement of the near-surface Panama Rock dike, since a higher stress barrier decreases the thickness of the (shaded) region of radial σ_3 that this dike would have needed to traverse while preserving its radial orientation. While shallow magma chambers significantly raise the elevation of stress barriers near Akaroa's paleo-summit compared with deeper chambers, they do not strongly affect the elevation of the stress barrier further downslope where crater rim dikes were

emplaced (Figure S12 in Supporting Information S1). The highest stress barriers occur in response to the large volume increases required for tensile failure of chambers surrounded by rock with a thermally reduced (i.e., T-dep) Young's modulus (Figure 7a). However, this thermal weakening prevents all but the most oblate ($a_c = 0.5$) chambers from achieving tensile failure for $V_m \geq 5$ km^3, and only the most oblate ($a_c = 0.5$) and prolate ($a_c = 2$) chambers from reaching tensile failure for $V_m = 1$ km^3 (Goldman, 2022d). This finding is consistent with numerical results of Gregg et al. (2012) showing that larger magma chambers thermally buffer their walls against tensile failure. Since simulations with a large, shallow, oblate magma chamber produce stress fields conducive to crater rim dike emplacement over the largest parameter space, we conclude that these properties represent the best-fit configuration for Akaroa's shallow magma plumbing system.

It should be noted that volume changes required for tensile failure in most of this study's simulations correspond with values of overpressure, defined as the pressure above lithostatic equilibrium (Supporting Information S1) that exceed 40 MPa, a value commonly treated in modeling studies of both basaltic and silicic magma plumbing systems as the upper limit for what is geologically feasible (e.g., Cabaniss et al., 2020; Gregg et al., 2012; Jellinek & DePaolo, 2003). This value derives from scaling arguments provided by Rubin (1995) in calculating the pressure required for magma to intrude a preexisting crack. For this study, however, the host rock is assumed to be unfractured prior to chamber inflation since our FEM cannot simulate crack propagation. This assumption also avoids the problem of arbitrarily defining the location of any chamber-proximal fractures that may have existed prior to crater rim dike emplacement, since we do not have the data to constrain these locations. Although overpressures >40 MPa are not commonly used in studies modeling magma plumbing systems (Karlstrom et al., 2009), they are necessary for chamber wall-rock failure under geologically plausible conditions (Gerbault, 2012; Grosfils et al., 2015) and consistent with geodetic observations of the Long Valley Caldera magma plumbing system (Newman et al., 2001). The Supporting Information (S1) contains additional justification for the magma pressures calculated in this study.

5.2. Timing of Edifice Construction and Dike Emplacement

The bulge-lithosphere-equilibrated and completely-equilibrated pre-stress conditions represent the short- and long-term endmembers of Akaroa Volcano's construction, respectively, but do not directly measure the volcano's growth rate. However, Stipp and McDougall (1968) and Timm et al. (2009) provide geologically plausible short- and long-term growth rates, respectively, for Akaroa that are consistent with the 0.1–1.0 Myr formation time for shield-shaped composite volcanoes (de Silva & Lindsay, 2015). Assuming a maximum volume of 3700 km^3 for Akaroa (based on the FEM model geometry, Figure 3), the average growth rate for "rapid", 0.1 Myr growth would have been 37 km^3/kyr, while the average "slow" 1 Myr growth rate would have been 3.7 km^3/kyr. Akaroa's rapid growth rate estimate is comparable to the average growth rate of 40 km^3/kyr for Hawaii's Kīlauea Volcano (Lipman & Calvert, 2013), while Akaroa's slow growth rate is comparable to the average 1.6 km^3/kyr rate of Sicily's Mt. Etna (Barreca et al., 2018).

The fact that most model configurations with a bulge-lithosphere-equilibrated prestress produce stress barriers within elevations where crater rim dikes are observed (Figures 5–7) strongly suggests that Akaroa Volcano was rapidly, rather than gradually, constructed. Conversely, model configurations with a completely-equilibrated prestress, which assume a gradually constructed edifice, produce no stress barrier for vertically ascending dikes to deflect along (Figure 7b). It should be noted that completely-equilibrated model configurations with an oblate magma chamber are still consistent with the emplacement of some crater rim dikes, since chambers with an aspect ratio $a_c < 1$ rupture at a sub-horizontal to outwardly ascending angle conducive to the propagation and emplacement of crater rim dikes without deflection along a stress barrier (c.f., Figure 5, path iv). However, bulge-lithosphere-equilibrated model configurations containing a large oblate magma chamber (Figure 7a) provide more pathways for dikes to reach the crater rim than their completely-equilibrated counterparts (Figure 7b). Thus, the FEM results most strongly support dike emplacement having occurred shortly after the completion of rapid, 0.1 Myr edifice growth.

While providing support for the rapid growth endmember of Akaroa's formation, this study's FEM simulations do not strictly rule out dike emplacement on intermediate timescales between 0.1 and 1.0 Myr. Specifically, the static, single timestep bulge-lithosphere-equilibrated simulations do not constrain how quickly dike emplacement occurred following rapid edifice construction. However, several individual static bulge-lithosphere-equilibrated results may indirectly represent how Akaroa's stress barrier evolved throughout its active lifespan if each model

configuration represents a phase in the evolution of Akaroa's shallow magma plumbing system. For example, growth of the main magma chamber feeding the crater rim dikes can be indirectly represented by comparing the stress fields of magma chambers of increasing size (Figure 6). The amount of time necessary to grow the largest modeled chamber (15 km^3) is on the order of 15 kyr, assuming an average input magma flux of 10^{-3} km^3/yr as modeled by Annen et al. (2014) for the analogous Soufrière Hills Volcano. Additionally, comparing the stress fields produced by model configurations with a constant versus T-dep Young's modulus (Figures 7a and 7b) may illustrate changes in the rate of input magma flux over time. This postulation is based on the numerical modeling results of Annen et al. (2006) that high magma fluxes produce large "aureoles" of thermally altered country rock, analogous to simulating a T-dep, thermally weakened host rock Young's modulus in the current study. While calculating the magma fluxes necessary to reproduce each T-ind or T-dep model configuration is beyond the scope of this study, the approach may be worth incorporating into future numerical modeling studies of magma plumbing systems.

The most direct way this study's FEM constrains the timing of dike emplacement is through time-dependent simulations of viscoelastic relaxation, specifically for the T-dep model (Figure 8). The T-ind model (Figure 7c) does not produce significant changes to the stress barrier in the vicinity of the crater rim between the initial elastic and fully relaxed viscoelastic endmembers. Although applying T-dep viscoelastic relaxation does not produce stress barrier elevations as high as those observed in the elastic, bulge-lithosphere-equilibrated model, simulating T-dep viscoelastic relaxation over multiple timesteps reveals that stress barrier elevation is correlated with the degree of relaxation (i.e., length of time passed, Figure 8). These simulations also indicate that applying the more realistic, temperature-dependent viscoelastic rheology to Akaroa and its underlying lithosphere lowers the stress barrier elevation overall compared with the purely elastic, and thus T-ind, model. This is especially true for magma chambers smaller than 15 km^3 (Figure 8a) or with non-oblate geometries (Figure 8d).

Another insight provided by the T-dep viscoelastic model is the rapid descent of the stress barrier by several hundred meters relative to the t = 0 elastic step within the first year of the simulation, followed by a slower descent within the first 1 kyr (Figure S14 in Supporting Information S1). This rapid initial descent of the stress barrier in the T-dep viscoelastic model weakens the argument that crater rim dikes were only emplaced shortly after construction of the entire Akaroa edifice, despite the consistency of the purely elastic model configuration with field and petrographic crater rim dike data. The time-dependent evolution of the stress barrier elevation, particularly the rapid descent followed by a logarithmically slowing ascent, can be attributed to the progressive upward relaxation of the model host rock, with the hottest, deepest rocks near the base of the lithosphere relaxing immediately due to their low viscosities, while shallower, cooler rocks relaxed over exponentially greater timescales (c.f., Equations S8–S13 in Supporting Information S1). However, the magnitude of stress barrier descent, as well as subsequent ascent, is significantly reduced for model configurations with a large, oblate chamber (Figures 8b and 8c), which still produce stress barrier locations within the region of crater rim dikes. Thus, the T-dep viscoelastic model provides additional evidence that Akaroa's crater rim dikes were fed by a large, oblate magma chamber.

5.3. Flexural History and Lithospheric "Bulge"

Akaroa's growth is expected to have caused downward flexure of the lithosphere due to the volcano's large radius (40 km) and the moderate, but not large, thickness of the underlying, elastically deforming region of the lithosphere (30 km). However, flexural model configurations produce stress fields dominated by radially oriented σ_3, preventing radial dike propagation and emplacement (Figure 7d). This discrepancy is most likely explained by the FEM applying edifice loading in a single timestep rather than incrementally. Le Corvec and McGovern (2018) demonstrate that stress fields calculated from the incremental construction of a large volcanic edifice are more conducive to the propagation of shallow radial dikes than from a volcano built in a single timestep, though their model does not include a pressurized shallow magma chamber. While outside the scope of the current study, simulating Akaroa's construction in multiple timesteps may yield stress field calculations that do allow shallow radial diking to occur, which would lend support to the gradual, 1 Myr edifice growth timescale presented by Timm et al. (2009).

It is also possible that conditions at the base of the lithosphere may have prevented significant flexure if mantle upwelling resulting from lithospheric delamination occurred (Timm et al., 2009). In fact, Timm et al. (2009) hypothesize that the Banks Peninsula's volcanism was fueled by post-delamination uplift of the lithosphere.

Therefore, the 70-km wide bulge of raised basement material beneath the Banks Peninsula may have been pushed upward by an underlying mass of upwelled asthenosphere. However, testing this hypothesis is outside the scope of the current study since the upwelled asthenosphere replaced portions of the preexisting lithosphere, a process that this study's spatially continuous FEM cannot simulate.

Understanding the formation of the lithospheric bulge beneath Akaroa Volcano is necessary for explaining the shallow, slope-parallel shape of the stress barrier for most elastic and viscoelastic model configurations (Figure S11 in Supporting Information S1). If not a product of asthenospheric upwelling, this bulge may be related to the formation of the Cretaceous Mid Canterbury Horst, an east-to-west-trending fault block that extends from the Canterbury Plains through the Banks Peninsula (Ring & Hampton, 2012). The pre-Cenozoic age of this horst is consistent with the modeling assumption of lithostatic equilibration between the bulge and underlying lithosphere prior to edifice construction in the Miocene. Moreover, the difference in elevation between the Torlesse greywacke basement beneath the Banks Peninsula and the Canterbury Plains sediments located just northwest of Lyttelton (Lee et al., 2017, Figure 12) is roughly consistent with the location of the northern fault boundary of the horst (Ring & Hampton, 2012, Figure 2). In fact, Ring and Hampton (2012) argue that the Mid Canterbury Horst spatially constrained Banks Peninsula volcanism, specifically by focusing volcanism along the intersection between the horst and local faults. Although this study's FEM does not incorporate local faults, it demonstrates a causal link between the presence of a conical lithospheric bulge, which spatially coincides with the Mid Canterbury Horst, and the occurrence of a stress barrier near the edifice surface, rather than at its base (Hurwitz et al., 2009; Poland et al., 2008). Based on the evidence provided by Timm et al. (2009) and Ring and Hampton (2012), it is possible that a combination of the Mid Canterbury Horst and post-delamination uplift contributed to the formation of the conical bulge.

6. Conclusions

This study combines field, petrographic, and seismic data from New Zealand's Akaroa Volcano with a finite element model (FEM) to investigate the volcanic system's paleo-stress field. Field mapping indicates that the dikes exposed along Akaroa's erosional crater rim have predominantly radial orientations and are found within a narrow elevation range, suggesting the existence of a stress barrier along which ascending, radially aligned dikes deflected before emplacement. Numerical simulations of the Akaroa system suggest that the edifice was constructed relatively quickly (within 0.1 Myr), while dikes were emplaced either shortly after edifice construction or throughout Akaroa's remaining ~1 Myr eruption lifespan. This study builds upon previous elastic, non-flexural, T-ind FEM studies of large composite and shield volcano systems by demonstrating how stress fields are affected by (a) the existence of a sloping, rather than flat, initial surface upon which the volcano is constructed, (b) a T-dep Young's modulus near the magma chamber wall, (c) viscoelastic relaxation (for model configurations with or without a geothermal gradient), and (d) flexure at the base of the lithosphere. This study's results can be further tested and refined through FEM simulations incorporating the sequential, rather than instantaneous, construction of Akaroa Volcano, as well as the temporal evolution of the magma plumbing system that produced Akaroa's crater rim dikes. More generally, FEMs building off this study's approach of mapping potential dike pathways through calculated principal stress orientations can complement geologic and geophysical data from active volcanoes to improve assessment of the hazards they may pose to nearby populations.

Data Availability Statement

Finite element model creation, simulations, and output results for this study were performed in *COMSOL Multiphysics version 5.5*, with the Structural Mechanics and Heat Transfer modules installed, available with a paid COMSOL license at https://www.comsol.com/. Input text files used for FEM simulations are available on FigShare (Goldman, 2022e). Results of FEM calculations of magma chamber pressure, volume change, and tensile failure location, as well as stress field visualizations exported from COMSOL, are also available on FigShare (Goldman, 2022c, 2022d). Additionally, field observations of Akaroa's dikes, including those located along the volcano's crater rim, and the ArcMap parent file, shapefiles, and other datasets used to generate the maps in Figure 1 and produce the topographic profile used in the FEM are available on FigShare (Goldman, 2022a, 2022b). The ArcMap file Akaroa_JGR_map.mxd and its associated shapefiles and data were generated in *ArcGIS Desktop version 10.7.1*, available with a paid license at https://www.esri.com/.

References

Albarède, F. (1993). Residence time analysis of geochemical fluctuations in volcanic series. *Geochimica et Cosmochimica Acta*, *57*(3), 615–621. https://doi.org/10.1016/0016-7037(93)90372-4

Anderson, E. M. (1939). XVII.—The dynamics of sheet intrusion. *Proceedings of the Royal Society of Edinburgh*, *58*, 242–251. https://doi.org/10.1017/S0370164600011159

Annen, C., Paulatto, M., Sparks, R. S. J., Minshull, T. A., & Kiddle, E. J. (2014). Quantification of the intrusive magma fluxes during magma chamber growth at Soufriere Hills Volcano (Montserrat, Lesser Antilles). *Journal of Petrology*, *55*(3), 529–548. https://doi.org/10.1093/petrology/egt075

Annen, C., Scaillet, B., & Sparks, R. S. J. (2006). Thermal constraints on the emplacement rate of a large intrusive complex: The Manaslu Leucogranite, Nepal Himalaya. *Journal of Petrology*, *47*(1), 71–95. https://doi.org/10.1093/petrology/egi068

Baer, G., & Reches, Z. (1987). Flow patterns of magma in dikes, Makhtesh Ramon, Israel. *Geology*, *15*(6), 569–572. https://doi.org/10.1130/0091-7613(1987)15<569:FPOMID>2.0

Bagnardi, M., & Amelung, F. (2012). Space-geodetic evidence for multiple magma reservoirs and subvolcanic lateral intrusions at Fernandina Volcano, Galápagos Islands. *Journal of Geophysical Research*, *117*(B10406). https://doi.org/10.1029/2012JB009465

Barreca, G., Branca, S., & Monaco, C. (2018). Three-dimensional modeling of mount Etna Volcano: Volume Assessment, trend of eruption rates, and geodynamic significance. *Tectonics*, *37*(3), 842–857. https://doi.org/10.1002/2017TC004851

Bertolett, E. M. (2019). *Understanding the Akaroa magmatic system: A multi-method approach to erupted plutonic lithics (Doctoral dissertation)*. University of Canterbury. https://doi.org/10.26021/9265

Brenna, M., Price, R., Cronin, S. J., Smith, I. E. M., Sohn, Y. K., Kim, G. B., & Maas, R. (2014). Final magma storage depth modulation of explosivity and Trachyte–Phonolite Genesis at an Intraplate Volcano: A case study from Ulleung Island, South Korea. *Journal of Petrology*, *55*(4), 709–747. https://doi.org/10.1093/petrology/egu004

Cabaniss, H. E., Gregg, P. M., & Grosfils, E. B. (2018). The role of tectonic stress in triggering large silicic caldera eruptions. *Geophysical Research Letters*, *45*(9), 3889–3895. https://doi.org/10.1029/2018GL077393

Cabaniss, H. E., Gregg, P. M., Nooner, S. L., & Chadwick, W. W. (2020). Triggering of eruptions at axial seamount, Juan de Fuca Ridge. *Scientific Reports*, *10*(1), 10219. https://doi.org/10.1038/s41598-020-67043-0

Chestler, S. R., & Grosfils, E. B. (2013). Using numerical modeling to explore the origin of intrusion patterns on Fernandina Volcano, Galapagos Islands, Ecuador. *Geophysical Research Letters*, *40*(17), 4565–4569. https://doi.org/10.1002/grl.50833

Corbi, F., Rivalta, E., Pinel, V., Maccaferri, F., Bagnardi, M., & Acocella, V. (2015). How caldera collapse shapes the shallow emplacement and transfer of magma in active volcanoes. *Earth and Planetary Science Letters*, *431*, 287–293. https://doi.org/10.1016/j.epsl.2015.09.028

de Silva, S., & Lindsay, J. M. (2015). Chapter 15—Primary volcanic landforms. In H. Sigurdsson (Ed.), *The Encyclopedia of volcanoes* (2nd edn, pp. 273–297). Academic Press. https://doi.org/10.1016/B978-0-12-385938-9.00015-8

Del Negro, C., Currenti, G., & Scandura, D. (2009). Temperature-dependent viscoelastic modeling of ground deformation: Application to Etna volcano during the 1993–1997 inflation period. *Physics of the Earth and Planetary Interiors*, *172*(3–4), 299–309. https://doi.org/10.1016/j.pepi.2008.10.019

Dorsey, C. J. (1988). *The geology and geochemistry of Akaroa volcano, Banks Peninsula, New Zealand (Doctoral dissertation)*. University of Canterbury. Retrieved from https://ir.canterbury.ac.nz/handle/10092/7524

Forsyth, P. J., Barrell, D. J. A., & Jongens, R. (2008). *Geology of the Christchurch area*. Lower Hutt: Institute of Geological and Nuclear Sciences. Retrieved from http://shop.gns.cri.nz/qchristchurch-zip/

Galgana, G. A., Grosfils, E. B., & McGovern, P. J. (2013). Radial dike formation on Venus: Insights from models of uplift, flexure and magmatism. *Icarus*, *225*(1), 538–547. https://doi.org/10.1016/j.icarus.2013.04.020

Galland, O., Burchardt, S., Hallot, E., Mourgues, R., & Bulois, C. (2014). Dynamics of dikes versus cone sheets in volcanic systems. *Journal of Geophysical Research: Solid Earth*, *119*(8), 6178–6192. https://doi.org/10.1002/2014JB011059

Gerbault, M. (2012). Pressure conditions for shear and tensile failure around a circular magma chamber; insight from elasto-plastic modelling. *Geological Society, London, Special Publications*, *367*(1), 111–130. https://doi.org/10.1144/SP367.8

Global Volcanism Program. (2021a). Report on La Palma (Spain). In S. K. Sennert (Ed.), *Weekly volcanic Activity Report, 15 September–21 September 2021*. Smithsonian Institution and U.S. Geological Survey. Retrieved from https://volcano.si.edu/ShowReport.cfm?doi=10.5479/si.GVP.WVAR20210519-223030

Global Volcanism Program. (2021b). Report on Nyiragongo (DR Congo). In S. K. Sennert (Ed.), *Weekly volcanic Activity Report, 19 May-25 May 2021*. Smithsonian Institution and U.S. Geological Survey. Retrieved from https://volcano.si.edu/ShowReport.cfm?doi=10.5479/si.GVP.WVAR20210519-223030

Goldman, R. (2022a). Akaroa JGR ArcMap files [Dataset]. Figshare. https://doi.org/10.6084/m9.figshare.19286900.v1

Goldman, R. (2022b). CraterRimDikeData.xlsx [Dataset]. Figshare. https://doi.org/10.6084/m9.figshare.19285505.v1

Goldman, R. (2022c). Parameter sweep GIFs [Dataset]. Figshare. https://doi.org/10.6084/m9.figshare.19287380.v1

Goldman, R. (2022d). Parameter_Sweep_Model_Results.xlsx [Dataset]. Figshare. https://doi.org/10.6084/m9.figshare.19285469.v2

Goldman, R. (2022e). Parametric Sweep input files [Dataset]. Figshare. https://doi.org/10.6084/m9.figshare.19287386.v1

Gregg, P. M., de Silva, S. L., Grosfils, E. B., & Parmigiani, J. P. (2012). Catastrophic caldera-forming eruptions: Thermomechanics and implications for eruption triggering and maximum caldera dimensions on Earth. *Journal of Volcanology and Geothermal Research*, *241–242*, 1–12. https://doi.org/10.1016/j.jvolgeores.2012.06.009

Grosfils, E. B. (2007). Magma reservoir failure on the terrestrial planets: Assessing the importance of gravitational loading in simple elastic models. *Journal of Volcanology and Geothermal Research*, *166*(2), 47–75. https://doi.org/10.1016/j.jvolgeores.2007.06.007

Grosfils, E. B., McGovern, P. J., Gregg, P. M., Galgana, G. A., Hurwitz, D. M., Long, S. M., & Chestler, S. R. (2015). Elastic models of magma reservoir mechanics: A key tool for investigating planetary volcanism. *Geological Society, London, Special Publications*, *401*(1), 239–267. https://doi.org/10.1144/SP401.2

Gudmundsson, A. (1990). Emplacement of dikes, sills and crustal magma chambers at divergent plate boundaries. *Tectonophysics*, *176*(3–4), 257–275. https://doi.org/10.1016/0040-1951(90)90073-H

Hampton, S. J., & Cole, J. W. (2009). Lyttelton Volcano, Banks Peninsula, New Zealand: Primary volcanic landforms and eruptive centre identification. *Geomorphology*, *104*(3–4), 284–298. https://doi.org/10.1016/j.geomorph.2008.09.005

Hampton, S. J., & Gravley, D. M. (2020). Field Trip 5: Banks Peninsula's best bits: Volcanology, research and geopark. In *Geosciences 2020: Field Trip guides* (pp. 42–67). Geoscience Society of New Zealand.

Harp, A. G. (2021). Magma propagation and emplacement within the central intrusive complex of Summer Coon stratovolcano, Colorado. *Journal of Volcanology and Geothermal Research*, *419*, 107372. https://doi.org/10.1016/j.jvolgeores.2021.107372

Harp, A. G., & Valentine, G. A. (2018). Emplacement controls for the basaltic-andesitic radial dikes of Summer Coon Volcano and implications for flank vents at stratovolcanoes. *Bulletin of Volcanology*, *80*(2), 16. https://doi.org/10.1007/s00445-018-1194-4

Hartung, E. (2011). *Early magmatism and the formation of a "Daly Gap" at Akaroa shield volcano, New Zealand (master's thesis)*. University of Canterbury. Retrieved from https://ir.canterbury.ac.nz/handle/10092/5584

Hurwitz, D. M., Long, S. M., & Grosfils, E. B. (2009). The characteristics of magma reservoir failure beneath a volcanic edifice. *Journal of Volcanology and Geothermal Research*, *188*(4), 379–394. https://doi.org/10.1016/j.jvolgeores.2009.10.004

Jellinek, A. M., & DePaolo, D. J. (2003). A model for the origin of large silicic magma chambers: Precursors of caldera-forming eruptions. *Bulletin of Volcanology*, *65*(5), 363–381. https://doi.org/10.1007/s00445-003-0277-y

Karlstrom, L., Dufek, J., & Manga, M. (2009). Organization of volcanic plumbing through magmatic lensing by magma chambers and volcanic loads. *Journal of Geophysical Research*, *114*(B10), B10204. https://doi.org/10.1029/2009JB006339

Le Corvec, N., & McGovern, P. J. (2018). The effect of Ocean loading on the growth of Basaltic Ocean Island Volcanoes and their magmatic plumbing system. *Frontiers of Earth Science*, *6*, 119. https://doi.org/10.3389/feart.2018.00119

Lee, R. L., Bradley, B. A., Ghisetti, F. C., & Thomson, E. M. (2017). Development of a 3D velocity model of the Canterbury, New Zealand, region for broadband ground-Motion simulation. *Bulletin of the Seismological Society of America*, *107*(5), 2131–2150. https://doi.org/10.1785/0120160326

Lewis, G. M., & Hampton, S. J. (2015). Visualizing volcanic processes in SketchUp: An integrated geo-education tool. *Computers & Geosciences*, *81*, 93–100. https://doi.org/10.1016/j.cageo.2015.05.003

Lipman, P. W., & Calvert, A. T. (2013). Modeling volcano growth on the Island of Hawaii: Deep-water perspectives. *Geosphere*, *9*(5), 1348–1383. https://doi.org/10.1130/GES00935.1

Lundgren, P., Berardino, P., Coltelli, M., Fornaro, G., Lanari, R., Puglisi, G., et al. (2003). Coupled magma chamber inflation and sector collapse slip observed with synthetic aperture radar interferometry on Mt. Etna volcano. *Journal of Geophysical Research*, *108*(B5), 2247. https://doi.org/10.1029/2001JB000657

Martí, J., Villaseñor, A., Geyer, A., López, C., & Tryggvason, A. (2017). Stress barriers controlling lateral migration of magma revealed by seismic tomography. *Scientific Reports*, *7*(1), 40757. https://doi.org/10.1038/srep40757

McGovern, P. J., Grosfils, E. B., Galgana, G. A., Morgan, J. K., Rumpf, M. E., Smith, J. R., & Zimbelman, J. R. (2015). Lithospheric flexure and volcano basal boundary conditions: Keys to the structural evolution of large volcanic edifices on the terrestrial planets. *Geological Society, London, Special Publications*, *401*(1), 219–237. https://doi.org/10.1144/SP401.7

Mériaux, C., & Lister, J. R. (2002). Calculation of dike trajectories from volcanic centers. *Journal of Geophysical Research: Solid Earth*, *107*(B4). https://doi.org/10.1029/2001JB000436

Nakamura, K. (1977). Volcanoes as possible indicators of tectonic stress orientation—Principle and proposal. *Journal of Volcanology and Geothermal Research*, *2*(1), 1–16. https://doi.org/10.1016/0377-0273(77)90012-9

Neri, M., Acocella, V., Behncke, B., Giammanco, S., Mazzarini, F., & Rust, D. (2011). Structural analysis of the eruptive fissures at Mount Etna (Italy). *Annals of Geophysics*, *54*(5). https://doi.org/10.4401/ag-5332

Neri, M., Acocella, V., Behncke, B., Maiolino, V., Ursino, A., & Velardita, R. (2005). Contrasting triggering mechanisms of the 2001 and 2002–2003 eruptions of Mount Etna (Italy). *Journal of Volcanology and Geothermal Research*, *144*(1–4), 235–255. https://doi.org/10.1016/j.jvolgeores.2004.11.025

Newman, A. V., Dixon, T. H., Ofoegbu, G. I., & Dixon, J. E. (2001). Geodetic and seismic constraints on recent activity at Long Valley Caldera, California: Evidence for viscoelastic rheology. *Journal of Volcanology and Geothermal Research*, *105*(3), 183–206. https://doi.org/10.1016/S0377-0273(00)00255-9

Pansino, S., & Taisne, B. (2019). How magmatic storage regions Attract and repel propagating Dikes. *Journal of Geophysical Research: Solid Earth*, *124*(1), 274–290. https://doi.org/10.1029/2018JB016311

Parfitt, E. A., & Head, J. W. (1993). Buffered and unbuffered dike emplacement on Earth and Venus: Implications for magma reservoir size, depth, and rate of magma replenishment. *Earth, Moon, and Planets*, *61*(3), 249–281. https://doi.org/10.1007/BF00572247

Peltier, A., Ferrazzini, V., Staudacher, T., & Bachèlery, P. (2005). Imaging the dynamics of dyke propagation prior to the 2000-2003 flank eruptions at Piton de La Fournaise, Reunion Island. *Geophysical Research Letters*, *32*(22). https://doi.org/10.1029/2005GL023720

Philpotts, A. R., & Asher, P. M. (1994). Magmatic flow-direction indicators in a giant diabase feeder dike, Connecticut. *Geology*, *22*(4), 363–366. https://doi.org/10.1130/0091-7613(1994)022<0363:mfdiia>2.3.co;2

Philpotts, A. R., & Philpotts, D. E. (2007). Upward and downward flow in a camptonite dike as recorded by deformed vesicles and the anisotropy of magnetic susceptibility (AMS). *Journal of Volcanology and Geothermal Research*, *161*(1–2), 81–94. https://doi.org/10.1016/j.jvolgeores.2006.11.006

Pietruszka, A. J., & Garcia, M. O. (1999). The size and shape of Kilauea Volcano's summit magma storage reservoir: A geochemical probe. *Earth and Planetary Science Letters*, *167*(3–4), 311–320. https://doi.org/10.1016/S0012-821X(99)00036-9

Poland, M. P., Fink, J. H., & Tauxe, L. (2004). Patterns of magma flow in segmented silicic dikes at Summer Coon volcano, Colorado: AMS and thin section analysis. *Earth and Planetary Science Letters*, *219*(1–2), 155–169. https://doi.org/10.1016/S0012-821X(03)00706-4

Poland, M. P., Moats, W. P., & Fink, J. H. (2008). A model for radial dike emplacement in composite cones based on observations from Summer Coon volcano, Colorado, USA. *Bulletin of Volcanology*, *70*(7), 861–875. https://doi.org/10.1007/s00445-007-0175-9

Porreca, M., Acocella, V., Massimi, E., Mattei, M., Funiciello, R., & Debenedetti, A. (2006). Geometric and kinematic features of the dike complex at Mt. Somma, Vesuvio (Italy). *Earth and Planetary Science Letters*, *245*(1–2), 389–407. https://doi.org/10.1016/j.epsl.2006.02.027

Puglisi, G., Bonforte, A., & Maugeri, S. R. (2001). Ground deformation patterns on Mount Etna, 1992 to 1994, inferred from GPS data. *Bulletin of Volcanology*, *62*(6–7), 371–384. https://doi.org/10.1007/s004450000112

Ring, U., & Hampton, S. (2012). Faulting in Banks Peninsula: Tectonic setting and structural controls for late Miocene intraplate volcanism, New Zealand. *Journal of the Geological Society*, *169*(6), 773–785. https://doi.org/10.1144/jgs2011-167

Rubin, A. M. (1995). Propagation of magma-filled cracks. *Annual Review of Earth and Planetary Sciences*, *23*(1), 287–336. https://doi.org/10.1146/annurev.ea.23.050195.001443

Rubin, A. M., & Pollard, D. D. (1987). Origins of blade-like dikes in volcanic rift zones. In R. W. Decker, T. L. Wright, & P. H. Stauffer (Eds.), *Volcanism in Hawaii: U.S. Geological Survey Professional Paper 1350* (pp. 1449–1470). United States Government Printing Office. Retrieved from https://pubs.usgs.gov/pp/1987/1350/pdf/chapters/pp1350_ch53.pdf

Sewell, R. J. (1988). Late Miocene volcanic stratigraphy of central Banks Peninsula, Canterbury, New Zealand. *New Zealand Journal of Geology and Geophysics*, *31*(1), 41–64. https://doi.org/10.1080/00288306.1988.10417809

Shelley, D. (1985). Determining paleo-flow directions from groundmass fabrics in the Lyttelton radial dykes, New Zealand. *Journal of Volcanology and Geothermal Research*, *25*(1–2), 69–79. https://doi.org/10.1016/0377-0273(85)90005-8

Shelley, D. (1987). Lyttelton 1 and Lyttelton 2, the two centres of Lyttelton Volcano. *New Zealand Journal of Geology and Geophysics*, *30*(2), 159–168. https://doi.org/10.1080/00288306.1987.10422180

Stipp, J. J., & McDougall, I. (1968). Geochronology of the Banks Peninsula Volcanoes, New Zealand. *New Zealand Journal of Geology and Geophysics*, *11*(5), 1239–1258. https://doi.org/10.1080/00288306.1968.10420260

Timm, C., Hoernle, K., van den Bogaard, P., Bindeman, I., & Weaver, S. (2009). Geochemical evolution of intraplate volcanism at Banks Peninsula, New Zealand: Interaction between asthenospheric and lithospheric melts. *Journal of Petrology*, *50*(6), 989–1023. https://doi.org/10.1093/petrology/egp029

Watanabe, T., Masuyama, T., Nagaoka, K., & Tahara, T. (2002). Analog experiments on magma-filled cracks: Competition between external stresses and internal pressure. *Earth Planets and Space*, *54*(12), e1247–e1261. https://doi.org/10.1186/BF03352453

Williams, D. M., Avery, V. F., Coombs, M. L., Cox, D. A., Horwitz, L. R., McBride, S. K., et al. (2020). U.S. Geological Survey 2018 Kīlauea Volcano eruption response in Hawai'i—After-action review (Report No. 2020–1041). https://doi.org/10.3133/ofr20201041

Williams, H. (1941). *Calderas and their origin*. University of California Press.